J|A|C|S
ARTICLES

Geometry for Self-Assembling of Spherical Hydrocarbon Cages with Methane Thiolates on Au(111)

Shintaro Fujii, Uichi Akiba, and Masamichi Fujihira*

Contribution from the Department of Biomolecular Engineering, Tokyo Institute of Technology,
4259 Nagatsuta Midori-ku, Yokohama, 226-8501, Japan

Received March 17, 2002

Abstract: An organodisulfide with a pair of adamantane moieties was synthesized, and its self-assembled monolayer (SAM) was formed on Au(111). The adamantane moieties are almost spherical and much bulkier than alkyl chains. The structure was characterized by scanning tunneling microscopy. Two-dimensional crystals of the SAM were found to be four orientationally different hexagonals with almost the same lattice constant with $4\sqrt{3}a/3$ and $7a/3$ ($a = 0.2884$ nm, the Au lattice constant). The structure is assigned to four of the high-order commensurate adlayers. The present study of geometry and energetics for self-assembling of such an organosulfur compound with spherical cages provides a new insight into the probable SAM structure of various thiolate derivatives on Au(111).

Introduction

Despite over a decade of work aimed at preparing and characterizing self-assembled monolayers (SAMs) of thiolates on Au(111), there still is not a clear understanding of the factors that govern their structure. In other words, it is difficult to predict what types of molecules will or will not form a highly organized structure on surfaces. To answer this question, one has to understand the driving force for the two-dimensional (2D) self-assembly, that is, molecule−molecule interaction and adsorbate−substrate interaction. However, such driving force for the self-assembly has been studied using only limited kinds of adsorbates. There have been few general arguments on the geometry and energetics of formation of a highly organized structure of adsorbates on Au(111) using other kinds of adsorbates.

The majority of papers in recent years deal with alkanethiols or their substituted analogues. So far, alkanethiols with dye[1−7] and fluorocarbon[8−15] moieties and organosulfur compounds with other bulky moieties[16−20] have been investigated. In the former adsorbates, the high flexibility of the alkyl chains serves as a geometrical buffer between order in the end group and order in the headgroup. Depending upon relative strengths between Au substrate−sulfur interaction and molecule−molecule interaction of the end functional groups, molecular order of SAMs can be dominated by the substrate−sulfur interaction[9,21] or by the molecule−molecule interaction.[1−7,10] When the substrate−sulfur interaction is dominating, the lattices of SAMs are commensurate with Au(111), while, when the molecule−molecule interaction is dominating, it is not necessary that the lattices be commensurate with Au(111). A typical example of the commensurate lattice is the $(\sqrt{3} \times \sqrt{3})R30°$ structure for *n*-alkanethiols.[8,22,23] In the $(\sqrt{3} \times \sqrt{3})R30°$ structure, molecular axes are tilted to increase the molecule−molecule interaction,[21,24] when the cross sectional area of the adsorbate is smaller than the area per molecule of the unit cell (0.217 nm^2). Recently, a variety of lattices of SAMs incommensurate with Ag(111)[25−29]

---

* To whom correspondence should be addressed. E-mail: mfujihir@bio.titech.ac.jp.

(1) Caldwell, W. B.; Campbell, D. J.; Chen, K.; Herr, B. R.; Mirkin, C. A.; Malik, A.; Durbin, M. K.; Dutta, P.; Huang, K. G. *J. Am. Chem. Soc.* **1995**, *117*, 6071.
(2) Wolf, H.; Ringsdorf, H.; Delamarche, E.; Takami, T.; Kang, H.; Michel, B.; Gerber, Ch.; Jaschke, M.; But, H.-J.; Bamberg, E. *J. Phys. Chem.* **1995**, *99*, 7102.
(3) Wesch, A.; Dannenberger, O.; Woll, Ch.; Wolff, J.; Buck, M. *Langmuir* **1996**, *12*, 5330.
(4) Wang, R.; Iyoda, T.; Jiang, L.; Hashimoto, K.; Fujishima, A. *Chem. Lett.* **1996**, 1005.
(5) Wang, R.; Iyoda, T.; Jiang, L.; Tryk, D. A.; Hashimoto, K.; Fujishima, A. *J. Electroanal. Chem.* **1997**, *438*, 213.
(6) Fox, M. A.; Wooten, M. D. *Langmuir* **1997**, *13*, 7099.
(7) Tamada, K.; Nagasawa, J.; Nakajima, F.; Abe, K.; Ishida, T.; Hara, M.; Knoll, W. *Langmuir* **1998**, *14*, 3264.
(8) Chidsey, C. E. D.; Loiacono, D. N. *Langmuir* **1990**, *6*, 682.
(9) Alves, C. A.; Porter, M. D. *Langmuir* **1993**, *9*, 3507.
(10) Liu, G. Y.; Fenter, P.; Chidsey, C. E. D.; Ogletree, D. F.; Eisenberger, P.; Salmeron, M. *J. Chem. Phys.* **1995**, *101*, 4301.
(11) Schonherr, H.; Ringsdorf, H.; Jaschke, M.; Butt, H.-J.; Bamberg, E.; Allinson, H.; Evans, S. D. *Langmuir* **1996**, *12*, 3898.
(12) Ishida, T.; Yamamoto, S.; Mizutani, W.; Motomatsu, M.; Tokumoto, H.; Hokari, H.; Azehara, H.; Fujihira, M. *Langmuir* **1997**, *13*, 3261.
(13) Schonherr, H.; Vancso, G. J. *Langmuir* **1997**, *13*, 3769.
(14) Tsao, M.-W.; Hoffmann, C. L.; Rabolt, J. F.; Johnson, H. E.; Castner, D. G.; Erdelen, C.; Ringsdorf, H. *Langmuir* **1997**, *13*, 4317.
(15) Tamada, K.; Ishida, T.; Knoll, W.; Fukushima, H.; Colorado, R., Jr.; Graupe, M.; Shmakova, O. E.; Lee, T. R. *Langmuir* **2001**, *17*, 1913.
(16) Kim, Y.-T.; Robin, L.; McCarley, R. L.; Bard, A. J. *J. Phys. Chem.* **1992**, *96*, 7416.
(17) Shi, X.; Caldwell, W. B.; Chen, K.; Mirkin, C. A. *J. Am. Chem. Soc*. **1994**, *116*, 11598.
(18) Katsumata, S.; Ide, A. *Jpn. J. Appl. Phys.* **1994**, *33*, 3723.
(19) Katsumata, S.; Ide, A. *Jpn. J. Appl. Phys.* **1995**, *34*, 3360.
(20) Mizutani, W.; Motomatsu, M.; Tokumoto, H. *Thin Solid Films* **1996**, *273*, 70.
(21) Sellers, H.; Ulman, A.; Shnidman, Y.; Eilers, J. E. *J. Am. Chem. Soc.* **1993**, *115*, 9389.
(22) Strong, L.; Whitesides, G. M. *Langmuir* **1988**, *4*, 546.
(23) Chidsey, C. E. D.; Liu, G. Y.; Rowntree, P.; Scoles, G. *J. Chem. Phys.* **1989**, *91*, 4421.
(24) Nuzzo, R. G.; Dubois, L. H.; Allara, D. L. *J. Am. Chem. Soc*. **1990**, *112*, 558.
(25) Harris, A. L.; Rothberg, L.; Dubois, L. H.; Levinos, N. J.; Dhar, L. *Phys. Rev. Lett.* **1990**, *64*, 2086.
(26) Harris, A. L.; Rothberg, L.; Dubois, L. H.; Levinos, N. J.; Dhar, L. *J. Chem. Phys.* **1991**, *94*, 2438.

10.1021/ja026214t CCC: $22.00

or Au(111)[30−34] have also been reported. Such bulky functional groups as fluorocarbon occupy the larger areas per molecule than 0.217 nm^2 and can be commensurate or incommensurate depending upon dominancy between the two types of interactions. The highly commensurate lattice of the 2×2 structure was reported for the SAM of $CF_3(CF_2)_7(CH_2)_2SH$ on Au(111),[9] while the high-order commensurate $c(7 \times 7)$ structure was also observed for SAMs of $CF_3(CF_2)_n(CH_2)_2SH$ ($n = 11$, 7, and 5) on Au(111).[10]

Recently, we have reported a scanning tunneling microscopy (STM) study of SAMs of disulfides with bicyclo[2.2.2]octane moieties with an H− or a Cl− end group on Au(111).[35] The STM images reflect the structure of SAMs of this spherical bulky rigid moiety. Linear rods having bicyclo[2.2.2]octyl units as well as bicyclo[2.2.2]octane were reported to have much higher melting points[36] than *n*-alkanes with similar molecular lengths. This indicates that the van der Waals molecule−molecule interaction between bicyclo[2.2.2]octane moieties is much higher than that between alkyl chains with similar molecular lengths. In addition, for such spherical end groups, a gain in the molecule−molecule interaction cannot be attained by tilting. Therefore, if the molecule−molecule interaction is dominating, the lattice constant of the SAM will be determined by the size of the end group. However, energetics and geometrical factors determining the SAM structure for such spherical and bulky end groups have not been clarified yet.

In the present study, an organosulfur compound with tricyclo-[3.3.1.1^{3,7}]decane (adamantane) that is another bulky cage hydrocarbon has been synthesized, and its overlayer structure on Au(111) has been characterized using STM in air and in ultrahigh vacuum (UHV). This adsorbate has a methylene group between an adamantane end group and a sulfur binding atom that provides flexibility in orientation of the adsorbate.[37,38] The adamantane moiety also has a spherical shape whose size is slightly larger than that of bicyclo[2.2.2]octane. One of the characteristic features of adsorbates with cage hydrocarbon moieties is their rigidity of the bulky end groups. Finally, energetics and the geometrical factors for the SAM formation on Au(111) are discussed by taking account of recent theoretical developments[21,39−47] in the substrate−sulfur interaction and by introducing a method to find out the most stable molecular order among possible SAM structures on Au(111).

Scheme 1

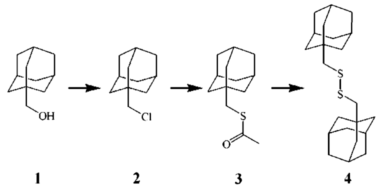

Experimental Section

(i) Syntheses. Compound **4** in Scheme 1 was newly synthesized from commercially available tricyclo[3.3.1.1^{3,7}]-decane-1-methanol **1** by a three-step procedure.

1-Chloromethyltricyclo[3.3.1.1^{3,7}]decane, 2. To a flask containing **1** (300 mg, 1.80 mmol) and dry CCl_4 (2 mL) was added triphenyl phosphine (520 mg, 1.98 mmol) under N_2 atmosphere. The mixture was refluxed 18 h. Excess solvent was removed in vacuo. The residue was dissolved in ether, filtered through a pad of Celite, concentrated in vacuo, and purified by column chromatography on silica gel (ether−hexane, 1:10) to give **2** (300 mg, 1.62 mmol) in 90% yield. ^{1}H NMR (300 MHz, $CDCl_3$): δ 3.22 (2H, s, CH_2Cl), 2.01 (3H, m, CH), 1.56−1.74 (12H, m, CH_2).

1-Thioacetylmethyltricyclo[3.3.1.1^{3,7}]decane, 3. A mixture of **2** (300 mg, 1.62 mmol) in dry DMF (1 mL) and potassium thioacetate (350 mg, 2.44 mmol) was refluxed for 48 h under N_2 atmosphere. After addition of water, the mixture was extracted with ether and concentrated in vacuo. The resulting mixture was purified by column chromatography on silica gel (ether−hexane, 1:10) to give **3** (160 mg, 0.71 mmol) in 43% yield. ^{1}H NMR (300 MHz, $CDCl_3$): δ 2.73 (2H, s, CH_2S), 2.34 (3H, s, CH_3), 1.97 (3H, m, CH), 1.50−1.71 (12H, m, CH_2).

Bis(tricyclo[3.3.1.1^{3,7}]decylmethyl)disulfide, 4. To a solution of **3** (160 mg, 0.71 mmol) in dry methanol (2 mL) was added KOH (200 mg), and the mixture was refluxed for 4 h. After addition of water, the mixture was refluxed for an additional 12 h and extracted with ether. The organic layer was combined, washed with brine, dried over $MgSO_4$, and concentrated in vacuo. The crude mixture was purified by column chromatography on silica gel (ether−hexane, 1:20) to give **4** (60 mg, 0.16 mmol) as a white powder in 46% yield. ^{1}H NMR (300 MHz, $CDCl_3$): δ 2.63 (4H, s, CH_2S), 1.97 (6H, m, CH), 1.57−1.72 (24H, m, CH_2). ^{13}C NMR (75 MHz, $CDCl_3$): δ 56.2, 41.9, 36.3, 34.3, 28.7. Anal. Calcd for $C_{22}H_{34}S_2$: C, 69.61; H, 9.74; S, 20.65. Found: C, 69.20; H, 10.13; S, 20.66. Mp = 66−67 °C.

(ii) Scanning Tunneling Microscopy. Au(111) surfaces for STM studies were prepared by thermal evaporation of gold (99.99%) onto freshly cleaved mica in vacuo with a background pressure of $<7 \times 10^{-5}$ Pa at 350−400 °C. SAMs were prepared by dipping the Au substrates for 10−72 h in 0.5 mM ethanol solutions of **4**. STM measurements were performed with a commercially available STM in air (DI: Nanoscope IIIa) and that in a UHV environment, that is, $<5 \times 10^{-8}$ Pa (JEOL: JSPM-4500S). All STM images were obtained using a constant-current mode with a tungsten tip at room temperature. The tunneling current, I_t, was set between 30 and 100 pA, and the sample bias voltage, V_b, was +0.5−+1.5 V. All of the images are unfiltered unless otherwise noted.

Results and Discussion

(i) Scanning Tunneling Microscopy in Air. Figure 1a shows a constant-current STM image of a 20×20 nm^2 area of a SAM

---

(27) Fenter, P.; Eisenberger, P.; Li, J.; Camillone, N., III; Bernasek, S.; Scoles, G.; Ramanarayanan, T. A.; Ling, K. S. *Langmuir* **1991**, *7*, 2013.

(28) Gui, J. Y.; Stern, D. A.; Frank, D. G.; Lu, F.; Zapien, D. C.; Hubbard, A. T. *Langmuir* **1991**, *7*, 955.

(29) Dhirani, A.; Hines, M. A.; Fisher, A. J.; Ismail, O.; Guyot, P. *Langmuir* **1995**, *11*, 2609.

(30) Jung, H. H.; Won, Y. D.; Shin, S.; Kim, K. *Langmuir* **1999**, *15*, 1147.

(31) Jin, Q.; Rodriguez, J. A.; Li, C. Z.; Darici, Y.; Tao, N. J. *Surf. Sci.* **1999**, *425*, 101.

(32) Wan, L.-J.; Terashima, M.; Noda, H.; Osawa, M. *J. Phys. Chem. B* **2000**, *104*, 3563.

(33) Yang, G.; Qian, Y.; Engtrakul, C.; Sita, L. R.; Liu, G. Y. *J. Phys. Chem. B* **2000**, *104*, 9059.

(34) Kang, J. F.; Ulman, A.; Liao, S.; Jordan, R.; Yang, G.; Liu, G.-Y. *Langmuir* **2001**, *17*, 95.

(35) Fujii, S.; Akiba, U.; Fujihira, M. *Chem. Commun.* **2001**, 1688.

(36) Zimmerman, H. E.; King, R. K.; Meinhardt, M. B. *J. Org. Chem.* **1992**, *57*, 5484.

(37) Tao, Y.-T.; Wu, C.-C.; Eu, J.-Y.; Lin, W.-L.; Wu, K.-C.; Chen, C.-H. *Langmuir* **1997**, *13*, 4018.

(38) Lavrich, D. J.; Wetterer, S. M.; Bernasek, S. L.; Scoles, G. *J. Phys. Chem. B* **1998**, *102*, 3456.

(39) Mar, W.; Klein, M. L. *Langmuir* **1994**, *10*, 188.

(40) Beardmore, K. M.; Kress, J. D.; Gronbech, N.; Bishop, A. R. *Chem. Phys. Lett.* **1998**, *286*, 40.

(41) Hakkinen, H.; Barnett, R. N.; Landman, U. *Phys. Rev. Lett.* **1999**, *82*, 3264.

(42) Gronbeck, H.; Curioni, A.; Andreoni, W. *J. Am. Chem. Soc.* **2000**, *122*, 3839.

(43) Yourdshahyan, Y.; Zhang, H. K.; Rappe, A. M. *Phys. Rev. B* **2001**, *63*, 081495(R).

(44) Hyashi, T.; Morikawa, Y.; Nozoye, H. *J. Chem. Phys.* **2001**, *114*, 7615.

(45) Akinaga, Y.; Nakajima, T.; Hirao, K. *J. Chem. Phys.* **2001**, *114*, 8555.

(46) Vargas, M. C.; Giannozzi, P.; Selloni, A.; Scoles, G. *J. Phys. Chem. B* **2001**, *105*, 9509.

(47) Kruger, D.; Fuchs, H.; Rousseau, R.; Marx, D.; Parrinello, M. *J. Chem. Phys.* **2001**, *115*, 4776.

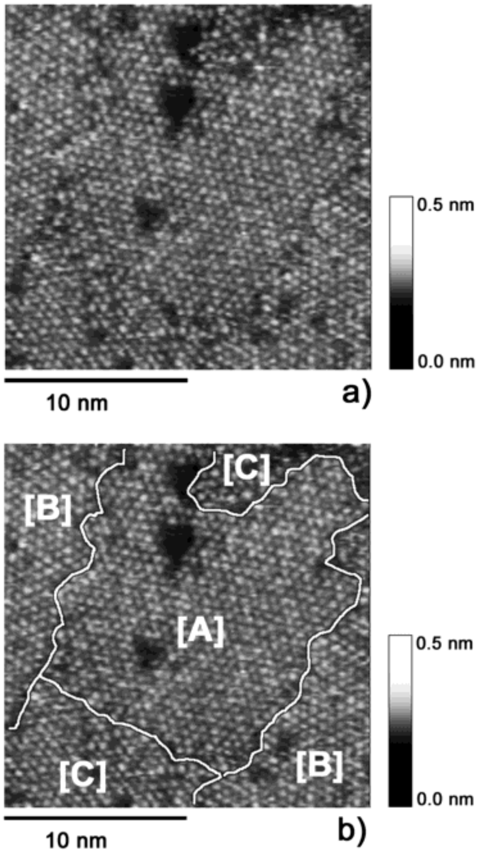

Figure 1. (a) A constant-current STM image of a 20 × 20 nm^2 area of a SAM of **4** on Au(111) ($I_t = 50$ pA, $V_b = +1$ V). (b) Assignment of domains in (a) into three groups: [A], [B], and [C] where the angles of molecular alignments are different. White letters and lines illustrate the domains and their boundaries, respectively.

of **4** on Au(111) observed in an atmospheric condition. The surface consists of domains of closely packed hexagonal phases, which have the same nearest neighbor spacing but have different rotational angles. To determine the lattice constant of the SAM of **4**, the lattice constant of a *n*-decanethiolate SAM known to form the $(\sqrt{3} \times \sqrt{3})R30°$ structure was used as a standard. Just after the STM image of the SAM of **4** was recorded, the *n*-decanethiolate SAM was scanned over the same range of its area using the same tip (not shown here). On the basis of the lattice constant of 0.499 nm for the *n*-decanethiolate SAM, the lateral distance in the STM image of the SAM of **4** was calibrated. After such a calibration, the lattice constant of the SAM of **4** was found to be 0.65 ± 0.02 nm. Now that the lattice constant of the SAM of **4** has been determined, we have to measure rotational angles among different domains in Figure 1a. From analyses of the angles described below, there are three different domains in terms of the rotational angles, that is, [A], [B], and [C] domains as shown in Figure 1b. To get rid of errors in determination of the rotational angles caused by thermal drift, hysteresis of piezo-scanner, and piezo-electric creep effect, the following care was taken. First, we attempted to keep the thermal drift as small as possible. Second, to avoid the hysteresis of piezo-scanner and the piezo-electric creep effect, relative angles between two different domains were measured using molecular arrays imaged in a short time, that is, in almost the same time domain. In other words, the angles were compared in the narrow *y* region on the image along the scan lines (parallel to *x* axis). In this way, the angle of the hexagonal lattice of an upper left domain [B] was found to rotate clockwise by 20 ± 3° with respect to (wrt) that of a centered domain [A], while that of the [B] domain in the bottom was found to rotate 40 ± 4° clockwise wrt that of the [C] domain in the bottom. As a result, the lattice of the [C] domain was found to rotate counterclockwise by 20 ± 4° wrt that of the [A] domain. The hexagonal lattice of the upper left domain [B] and that of the centered domain [A] were also found to rotate by 21 ± 3° and 1 ± 3° clockwise, respectively, wrt that of an underlying Au(111) surface by mechanically removing a part of the SAM in this [B] domain with the STM tip.

Table 1. Possible Candidates for Hexagonal Adlayers of SAMs of **4** on Au(111)

number	$\lvert a_n \rvert$	$\lvert a_n \rvert/2$	$\lvert a_n \rvert/3$	$\lvert a_n \rvert/4$	unit cell
1	0.288				1×1
2	0.498				$(\sqrt{3} \times \sqrt{3})R30°$
3	0.576				2×2
4*d*+	0.762				$(\sqrt{7} \times \sqrt{7})R + 19.12°$
4*d*−	0.762				$(\sqrt{7} \times \sqrt{7})R - 19.12°$
10*d*+		**0.660**			$(\sqrt{21} \times \sqrt{21})R + 10.89°$
10*d*−		**0.660**			$(\sqrt{21} \times \sqrt{21})R - 10.89°$
11		0.720			5×5
19			**0.665**		$(4\sqrt{3} \times 4\sqrt{3})R30°$
20′			**0.672**		7×7
20*d*+			**0.672**		$(7 \times 7)R + 21.79°$
20*d*−			**0.672**		$(7 \times 7)R - 21.79°$
21*d*+			0.692		$(2\sqrt{13} \times 2\sqrt{13})R + 13.90°$
21*d*−			0.692		$(2\sqrt{13} \times 2\sqrt{13})R - 13.90°$
22*d*+			0.725		$(\sqrt{57} \times \sqrt{57})R + 6.59°$
22*d*−			0.725		$(\sqrt{57} \times \sqrt{57})R - 6.59°$
33′*d*+				**0.687**	$(\sqrt{91} \times \sqrt{91})R + 5.21°$
33′*d*−				**0.687**	$(\sqrt{91} \times \sqrt{91})R - 5.21°$
33*d*+				**0.687**	$(\sqrt{91} \times \sqrt{91})R + 27.00°$
33*d*−				**0.687**	$(\sqrt{91} \times \sqrt{91})R - 27.00°$
34*d*+				0.694	$(\sqrt{93} \times \sqrt{93})R + 21.05°$
34*d*−				0.694	$(\sqrt{93} \times \sqrt{93})R - 21.05°$
35*d*+				0.709	$(\sqrt{97} \times \sqrt{97})R + 15.30°$
35*d*−				0.709	$(\sqrt{97} \times \sqrt{97})R - 15.30°$

From the structural analyses of the SAM of **4** in air, we can summarize that (1) the lattice constant is 0.65 ± 0.02 nm and (2) the rotational angles of the [A], [B], and [C] wrt the underlying gold atomic row are −1 ± 3°, −21 ± 3°, and +19 ± 4°, respectively. Here, the + sign in the rotational angle corresponds to counterclockwise rotation in the same way as used later in Table 1.

(ii) Scanning Tunneling Microscopy in UHV. (a) Calibration. To reduce thermal drift and an acoustic noise level that comes from atmosphere, STM measurements were also conducted under the UHV condition. STM images of Si(111)-7 × 7 and highly oriented pyrolytic graphite (HOPG) were used as standards of hexagonal lattices with lattice constants of 2.69 and 0.2456 nm, respectively. Those images showed somewhat distorted hexagonal lattices even when their drifts became negligibly small. The distortion is caused in general by the following factors: (i) decalibration of *x* and *y* axes, (ii) nonorthogonality of *x* and *y* direction of the scanner, (iii) the drift of the sample wrt the tip, and (iv) hysteresis and creep of the scanner. In the present UHV STM, negligibly small drift could be achieved by reducing thermal drift. The hysteresis can be neglected for the small scan ranges typical for atomic or molecular imaging. To avoid the creep effect, the distortion was corrected using the lower 3/4 parts of the STM images of the standard samples, because in the top parts of the images the lattices were elongated by the sudden change in *y* position.

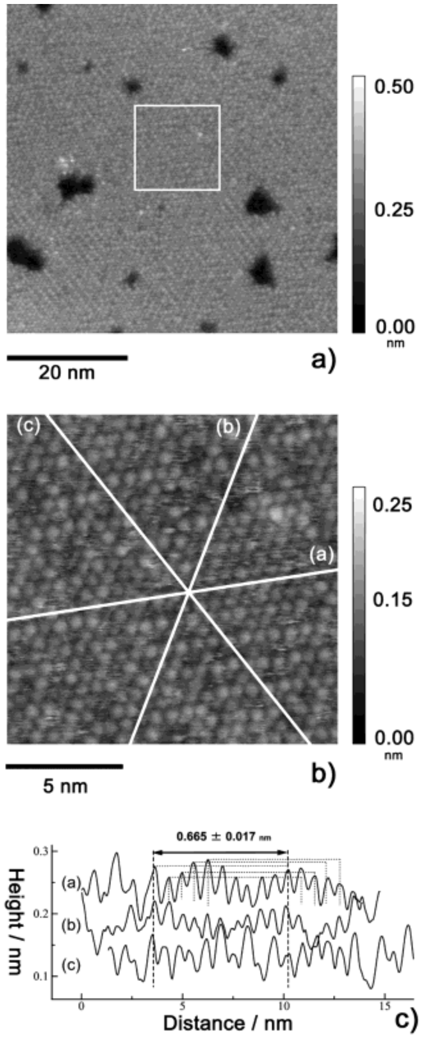

Figure 2. (a) and (b) Constant-current STM images of a 55 × 55 nm^2 and a 14 × 14 nm^2 area of a SAM of **4** on Au(111), respectively, in a UHV environment ($I_\mathrm{t} = 90$ pA, $V_\mathrm{b} = +1.0$ V). (c) Low pass filtered cross sectional profiles along the corresponding lines are shown in Figure 2b.

Finally, the distortion correction for the calibration factors and the nonorthogonality was carried out using a standard method[48−50] on the two standard samples. Using these correction factors, we measured the lattice constant of the *n*-decanethiolate SAM described above. The lattice constant of the SAM (($\sqrt{3} \times \sqrt{3}$)-$R30°$) was then found to be 0.504 ± 0.007 nm, and the observed lattice was hexagonal within the angle error of ±3°.

(b) Lattice Constant. Figure 2a show a 55 × 55 nm^2 STM image of a SAM of **4** on Au(111) in the UHV environment. This STM image as well as that shown in Figure 2b were obtained after the distortion correction described above. In the same way as in *n*-alkanethiolate SAMs, single Au atom deep pit defects are seen in Figure 2a as well as in Figure 1. Owing to the bulkiness and the spherical shape of the adamantane moieties, they are expected to be oriented almost perpendicularly to the substrate surface. Thus, the formation of the domain structure due to the tilt of adsorbates can be avoided.[35] By this reason, the structural domain boundaries observed for *n*-alkanethiolate SAMs[21,51−53] were not observed in Figure 2a. In addition, domains having different rotational angles observed in Figure 1 are not seen in Figure 2a. Only a single domain was observed in this image.

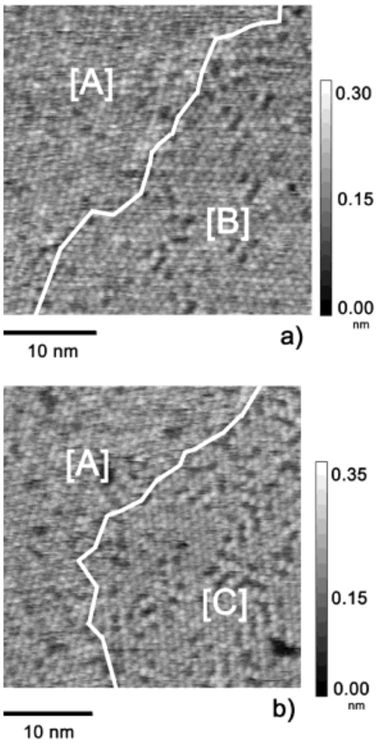

Figure 3. Constant-current STM images of 22 × 22 nm^2 areas of a SAM of **4** on Au(111) in a UHV environment ($I_\mathrm{t} = 35$ pA, $V_\mathrm{b} = +1.0$ V). Assignment of domains into three groups: [A], [B], and [C] where the angles of molecular alignments are different. White letters and lines illustrate the domains and their boundaries, respectively.

Figure 2b and c shows a 14 × 14 nm^2 STM image of the same domain of the SAM of **4** (that is marked by a white square in Figure 2a) and low pass filtered cross sectional profiles along three lines shown on the image, respectively. On the basis of the UHV STM experiment, the lattice constant of the SAM of **4** was determined to be 0.665 ± 0.017 nm. This value is close to the nearest neighbor distance of 0.667 ± 0.001 nm for 3D adamantane crystal.[54] As shown in Figure 2b, the lattice of the SAM of **4** was also found to be hexagonal within the angle error of ±3°.

(c) Rotational Angles. The rotational angles between domains were studied further in the UHV environment. Figure 3a and b shows STM images of a 22 × 22 nm^2 area of a SAM of **4** on the same terrace of Au(111) under the UHV condition. As shown in the images, there are domains [A] and [B] in Figure 3a, while domains [A] and [C] are in Figure 3b in terms of rotational angles. Distortions of the images in Figure 3 were restored by the same procedure as described above. The hexagonal lattice of the domain [B] in Figure 3a was found to rotate by 22.8 ± 3° clockwise wrt the domain [A]. The hexagonal lattice of the domain [C] in Figure 3b was found to rotate by 19.3 ± 3° counterclockwise wrt that of domain [A].[55]

---

(48) Cai, C. Z.; Chen, X. Y.; Shu, Q. Q.; Zheng, X. L. *Rev. Sci. Instrum.* **1992**, *63*, 5649.

(49) Jørgensen, J. F.; Madsen, L. L.; Garnaes, J.; Carneiro, K.; Schaumburg, K. *J. Vac. Sci. Technol., B* **1994**, *12*, 1702.

(50) Staub, R.; Alliata, D.; Nicolini, C. *Rev. Sci. Instrum.* **1995**, *66*, 2513.

(51) Bumm, L. A.; Arnold, J. J.; Cygan, M. T.; Dunbar, T. D.; Burgin, T. P.; Jones, L., II; Allara, D. L.; Tour, J. M.; Weiss, P. S. *Science* **1996**, *271*, 1705.

(52) Ulman, A. *Chem. Rev.* **1996**, *96*, 1533.

(53) Porier, G. E. *Chem. Rev.* **1997**, *97*, 1117.

(54) Nowacki, W. *Helv. Chim. Acta* **1945**, *28*, 1233.

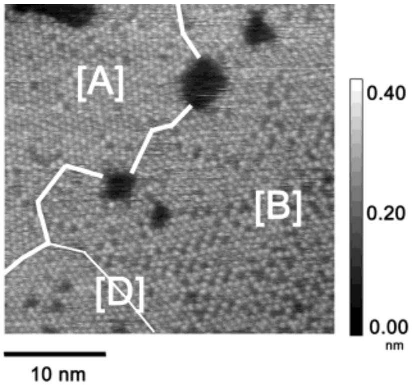

Figure 4. A constant-current STM image of a 35 × 35 nm^2 area of a SAM of **4** on Au(111) in a UHV environment ($I_t = 95$ pA, $V_b = +1.0$ V), in which a new domain [D] is seen.

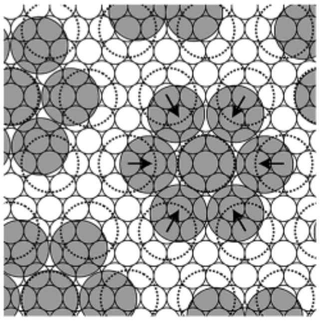

Figure 5. A drawing depicting "clustering" of a loosely packed SAM with (3 × 3) structure.

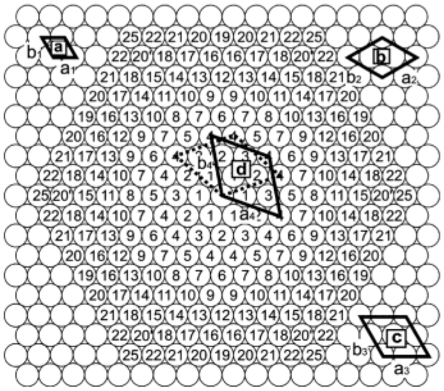

Figure 6. Illustration for calculation of lattice constants and rotational angles with respect to an underlying Au(111) lattice. Open circles represent Au atoms, and the numbers on the gold atoms indicate the order of increasing distances from a central atom. Two vectors from the central atom to two atoms with the number of 1, 2, 3, and 4 make unit cells of (a) a (1 × 1), (b) a ($\sqrt{3} \times \sqrt{3}$)R30°, (c) a (2 × 2), and (d) ($\sqrt{7} \times \sqrt{7}$)R + 19.12° and ($\sqrt{7} \times \sqrt{7}$)R − 19.12° adlayers, respectively.

It should be also noted that we found domain structures other than domains [A], [B], and [C]. Figure 4 shows a constant-current STM image of another 35 × 35 nm^2 area of a SAM of **4** on Au(111) under the UHV condition. In terms of rotational angles, there appear three domains [A], [B], and [D]. However, a boundary between domains [B] and [D] is not clearly demarcated. In addition, a lot of molecular defects are seen in this STM image, which is probably due to the UHV condition. The presence of the three domains, that is, competition among the three domains, is likely due to the high molecular defect density in the same way as shown in Figure 3a and b. The size of domains [B] and [D] and the boundary between them gradually changed during successive imaging. The hexagonal lattice of the domain [D] in Figure 4 was found to rotate by 31.4 ± 3° clockwise wrt the domain [A]. The domain [B] here rotates by 22.3 ± 3° clockwise wrt the domain [A].

The lattice constants of these four different domains were in good agreement with each other within their experimental errors of ±0.02 nm.

(iii) Geometrical Factors and Energetics for SAM Formation. Finally, we attempted to interpret why these orientation angles were observed among the hexagonal lattice of the SAM of **4** with the lattice constant of 0.665 ± 0.02 nm in the [A], [B], [C], and [D] domains on the underlying Au(111) surface ($a = 0.2884$ nm, the Au lattice constant).[53,56] In the following procedure to find the most appropriate structure of the present adsorbate **4** in terms of the adsorption energy, we will take the two contributions, that is, molecule−molecule interaction and Au substrate−sulfur interaction, into account. As to the substrate−sulfur interaction, we assume that the bridge site is the most stable, but the hollow site is also stable in comparison with the on-top site according to the recent theoretical studies.[21,39−47]

The lateral molecular−molecular interaction energy is minimized when the cross sectional molecular area of the adsorbate is equal to the area per molecule in the unit cell, with which the SAM would be formed. Because the gain in the molecule−molecule interaction cannot be attained by tilting for the spherical moieties as described above, the stabilization energy due to the molecular−molecular interaction decreases drastically with the increase in deviation of the nearest neighbor distance in the supposed SAM structure from the equilibrium distance of a 2D crystal of adamantane. The equilibrium distance is assumed to be close to the nearest neighbor distance of 0.667± 0.001 nm for a 3D adamantane crystal.[54] The increase in instability should be much more drastic when the supposed nearest neighbor distance is shorter than the equilibrium distance than when it is longer than the equilibrium distance because of the distance dependence of the 6−12 Lennard-Jones potential. The condition of the agreement between the supposed nearest neighbor and the equilibrium distance to find the possible stable SAM structure is not necessarily required when an energy gain by clustering is taken into account.[1] An example of clustering is shown in Figure 5, but this possibility is omitted in the following discussion, because the molecules are equally spaced in Figures 1−4.

In addition, we assumed that the optimized SAM structure should belong to a 2D hexagonal lattice, because the STM images of the SAM of **4** shown in Figures 1−4 show hexagonal lattices with different rotational angles. In other words, the arguments are restricted to the case of SAM formation with hexagonal lattices on Au(111). This can be applicable in general when the end groups are spherical.

In Figure 6, the hexagonal lattice of Au(111) is shown. The numbers on gold atoms indicate the order of increasing distances from a central atom. The smaller number corresponds to the shorter distance. Two vectors from the central atom to two atoms with the number of 1 make a unit cell of a (1 × 1) adlayer as

---

(55) We similarly analyzed angles between hexagonal lattices of different domains of an *n*-alkanethiolate SAM with the ($\sqrt{3} \times \sqrt{3}$)R30° structure described above. The angle analyses under the UHV condition showed that the angles between the different domains were 0° with an error of ±2°.

(56) Kittel, C. *Introduction to Solid State Physics*; John Wiley & Sons: New York, 1986.

shown in Figure 6a. Figure 6b−d corresponds to those of a ($\sqrt{3} \times \sqrt{3}$)R30°, a (2 × 2), and a ($\sqrt{7} \times \sqrt{7}$)$R + 19.12°$ (or ($\sqrt{7} \times \sqrt{7}$)$R - 19.12°$) adlayer, respectively.

In Table 1, hexagonal adlayers, which can be candidates for SAMs of **4**, are listed as well as the (1 × 1), ($\sqrt{3} \times \sqrt{3}$)R30°, and (2 × 2) adlayers. In the first column, the numbers on gold atoms forming the corresponding unit cells are listed. Subscripts $d+$ and $d-$ are used to show that there are two different unit cells with two different rotational angles. In the case of 20, there is another unit cell 20′ in addition to 20$d+$ and 20$d-$ with the same distance from the central atom. In the second column are listed the nearest neighbor distances in nanometers between adsorbates, where no additional adsorbates exist between the central and the numbered sites. In the third column are listed the averaged nearest neighbor distances between adsorbates, where one additional adsorbate is sandwiched between the central and the numbered sites. In this case, the additional adsorbate is incommensurate with Au(111). In the fourth and fifth columns, the nearest neighbor distances are listed for the cases where two and three additional incommensurate adsorbates are sandwiched between them, respectively. In the sixth column are listed the corresponding representations of the unit cells. The rotational angle corresponds to an angle between the molecular row of adsorbates and the underlying atomic rows of Au(111). Molecular lattices are omitted in Table 1 whose nearest neighbor distances are deviated significantly from the equilibrium distance of 0.667± 0.001 nm.

Among the commensurate molecular lattices in the second column, only 4$d+$ and 4$d-$ can be candidates. Yet, their nearest neighbor distance is too large. Among the high-order commensurate lattices in the third column, 10$d+$ and 10$d-$ can be the most likely candidates in terms of the nearest neighbor distance. Among the more high-order commensurate lattices in the fourth and fifth columns, 19, 20′, 20$d+$, 20$d-$, 33$d+$, 33$d-$, 33′$d+$, and 33′$d-$ can be the most likely candidates in terms of the nearest neighbor distances. In each column, the nearest neighbor distances for these most likely adlayers are represented in bold letters.

By taking account of the rotational angles among three different domains observed in Figures 1 and 3 (and those of the rotational angles of the adlayers wrt the underlying gold atomic row), we can determine the most probable adlayer structure among the most likely 10 candidates described above. As to the observed rotational angles in air, we summarized above that those of the [A], [B], and [C] wrt the underlying gold atomic row were −1 ± 3°, −21 ± 3°, and +19 ± 4°, respectively. The relation among the observed rotational angles in air was also confirmed by STM imaging in UHV as described above. Therefore, it can be concluded safely from comparison between these data and the calculated angles in Table 1 that the most probable adlayer structure in the domains [A], [B], and [C] is found to be 20′ (0°), 20$d-$ (−21.79°), and 20$d+$ (+21.79°). With these observed results, in good agreement with the model systems, in mind, we assigned the domain [D] described in the previous section to another most probable adlayer of 19. Within the experimental error of the lattice constant, the observed rotational angle of 31.4 ± 3° satisfies dramatically the calculated rotational angle of 30° for the 19 adlayer.

In Figure 7, the molecular lattice of the 20′ adlayer is illustrated by placing the spherical moieties of the commensurate adsorbates on the on-top sites of four corners of the diamond-like unit cell and placing the incommensurate adsorbates with equal spacing between these corner adsorbates without taking account of the favorable chemisorption sites of sulfur atoms on Au(111).

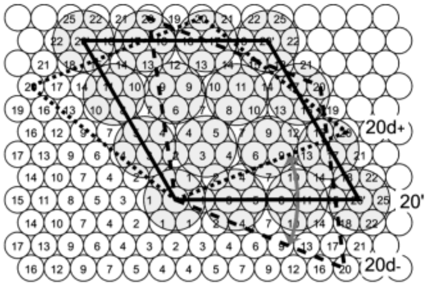

Figure 7. The most probable structure models of the high-order commensurate 20′, 20$d+$, and 20$d-$ adlayers of **4** on Au(111). Open circles and gray circles represent surface Au atoms and adsorbates, respectively.

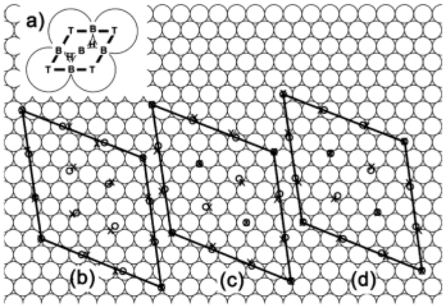

Figure 8. Three possible binding modes of sulfur atoms on Au(111) for the 20$d-$ adlayer. (a) Bridge (B), hollow (H), and on-top (T) sites in a gold (1 × 1) unit cell of Au(111). (b) An all bridge site mode (or a 9−0−0 mode) with four commensurate bridge sites at the corners of the unit cell, (c) a 6−2−1 mode with four commensurate hollow sites at the corners, and (d) another 6−2−1 mode with four commensurate on-top sites at the corners. The 9−0−0 mode is more favorable than the other two 6−2−1 binding modes due to the most highest binding energy and the highest surface density of the bridge sites as compared with those of the hollow and the on-top sites. Open circles form an equally spaced high-order commensurate molecular lattice, and crosses are the nearest sulfur binding sites on the bridge, the hollow, or the on-top sites of Au(111).

As described above so far, we demonstrate a method by which we determine the most probable adlayer structure among the most likely high-order commensurate adlayers in terms of the most favorable molecular−molecular distance, that is, the most favorable lateral molecular−molecular interaction. In other words, we took the substrate−sulfur interaction into account only in terms of the high-order commensurability. In this stage, we will discuss the contribution of the substrate−sulfur interaction to the total energy of adsorption in more detail. As shown in Figure 8a, the numbers of the bridge, the hollow, and the on-top sites per unit cell of Au(111) are 3, 2, and 1, respectively. In addition to this fact, the substrate−sulfur interaction is more favorable in terms of chemisorption energies in the order of the bridge, the hollow, and the on-top sites as described above.[21,39−47] The numbered sites in Figure 6 are not necessarily corresponding to the on-top sites when we search the commensurate or the high-order commensurate molecular lattices. Six equivalent bridge and six hollow sites surrounding all gold atoms can be shifted in parallel to one on-top site of all gold atoms. From these considerations, the bridge sites are most favorable in the high-order commensurate adlayers not only due to the chemisorption energy, but also due to the highest site density among the three different binding sites.

Figure 8b−d shows three types of possible binding sites for the 20*d*− adlayer structure. In Figure 8b, not only the commensurate adsorbates on the diamond corner but also other incommensurate adsorbates are illustrated to bind to bridge sites without large deviation from the equally spaced hexagonal molecular sites (an all bridge site mode or a 9−0−0 mode). In Figure 8c, the four corner commensurate binding sites are located in the hollow sites, while two incommensurate sites are located on one on-top and one hollow site without the deviation, and the other 10 incommensurate sites are on the bridge sites without the large deviation. Per unit cell, there are one on-top, two hollow, and six bridge sites (a 6−2−1 mode). Figure 8d shows another possible sulfur binding mode on Au(111). In this case, it is interesting to note that there are again one on-top, two hollow, and six bridge sites per unit cell (a 6−2−1 mode). Similar arguments are applicable to the 20*d*+ and 20′ adlayers. For the 19 adlayer, a 9−0−0 and a 0−6−3 mode are candidates for possible sulfur binding modes. Low probability in finding the SAM of **4** in the 19 adlayer geometry may be due to inferiority in the substrate−sulfur interaction, if any.

Because of the limit of the present STM systems, we could not distinguish these different binding modes, that is, the 9−0−0 (all bridge site) and the 6−2−1 mode for the 20′, 20*d*−, and 20*d*+ adlayers and the 9−0−0 and the 0−6−3 mode for the 19 adlayer, by the observed STM images. Differentiation of these binding modes by modifying the UHV STM to lower tunneling current levels will be studied soon.

Conclusions

For spherical adamantane moieties bound on Au(111), we attempted to find the most likely models, which satisfy the observed nearest neighbor distance, among possible high-order commensurate adlayers. The most probable models, 19, 20′, 20*d*+, and 20*d*− adlayers, satisfy not only the nearest neighbor distance but also the rotational angles of the molecular row against the underlying gold atoms row (i.e., 30°, 0°, +21.79°, and −21.79°, respectively). It is proposed in the frequently observed 20′, 20*d*+, and 20*d*− adlayers that all nine sulfur atoms in the unit cell bind to bridge sites of underlying gold atoms (the 9−0−0 mode), although the other binding mode (the 6−2−1 mode) cannot be ruled out. The present study supports experimentally the recent theoretical conclusion[21,39−47] that sulfur binding on the bridge sites is more favorable than that on the hollow sites in terms of their chemisorption energies. In addition, the chemisorption on the bridge sites is more favorable than that on the hollow sites in particular for the high-order commensurate adlayers, because the density of the bridge sites is 1.5 times higher than that of the hollow sites in Au(111), and thus deviation of the incommensurate bridge site from the ideal hexagonal molecular lattice can be shorter. Most of the sulfur atoms in these models are not commensurate with Au(111), but strain during anchoring on the incommensurate bridge sites is effectively released by a geometrical buffer played by a methylene bridge between the adamantane moiety and the sulfur binding atom.

Acknowledgment. This work was supported by a Grant-in-Aid for Scientific Research (A) (06403020, 11355036) from the Ministry of Education, Science, Sports, and Culture and a Grant-in-Aid for Creative Scientific Research on “Devices on molecular and DNA levels” (No. 13GS0017) from the Japan Society for the Promotion of Science.

JA026214T